

# Model Predictive Control for Multi-Port Modular Multilevel Converters in Electric Vehicles Enabling HESDs

Mohamed Badawy, Mohit Sharma, Carlos Hernandez, Ali-Elrattyah, and Joshua Coe

*Electrical Engineering Department, San Jose State University, San Jose, California, USA*

**Abstract**— In this paper, the authors propose a model predictive control (MPC) algorithm for multi-port modular multilevel converters (MP-MMCs). MP-MMCs are used to enable the use of hybrid energy storage devices (HESDs) in a scalable energy management system (EMS) for electric vehicle (EV) applications. HESDs refer to the use of multiple types of energy storage cells in an EV drivetrain system. In this paper, battery cells are sized for the EV energy density, while ultra-capacitor cells are used for high acceleration periods. This system reduces the EV drivetrain's weight and size due to eliminating high-power inverters and their filtering components. Using MPC, this system can achieve the following control objectives: 1) extend the battery cells lifetime and driving range by shielding them from high power pulses, 2) balance the state of charge levels of every storage cell, 3) increase the system efficiency through optimizing the supplied motor voltage and reducing the switching losses. Moreover, the proposed solution provides means for onboard high-power charging of EV storage cells. Finally, validation results are provided in the paper using a developed hardware prototype, co-simulations, and hardware in the loop system to verify the system's effectiveness.

**Index terms** – Battery management system, electric vehicles, electric vehicle drivetrain, hybrid energy storage devices, model predictive control, multilevel modular converters, ultracapacitors.

## I. INTRODUCTION

In recent years, hybrid and electric vehicles (HEV/EV) have witnessed widespread across the globe through continuous advancements in power electronic converters, energy storage systems, motor drives, and applicable control theories. However, several areas need further development to improve system efficiency, reduce cost, and extend vehicle life span. Proper selection and integration of energy storage systems do not only reduce the cost of HEV/EV, but they can also support motor operation at extended speed levels. Furthermore, the proper design/selection of power electronics drives helps achieve the required motor operation without overstressing the elements of energy storage systems. All these requirements cannot be attained without the development of an appropriate, effective control system.

### I.A). Hybrid Energy Storage Devices

HEVs/EVs' motors have high peak-to-average power requirements, which require special attention when designing system components to avoid system failure. Achieving high power and energy density using battery elements solely is feasible; however, that can be achieved through un-optimized design and components sizing [1]. Integrating batteries and ultra-capacitors (UCs) in a hybrid storage system is an effective solution for HEV/EV systems [2]. As indicated by Ragone plots, batteries can support high energy density at a reasonable cost. On the other hand, UCs can provide high power without any negative impact on their lifetime and lower losses [3]. Each of these storage devices has desirable features that match specific applications. For that purpose, hybrid energy storage devices (HESDs) composed of batteries and UCs are used in many applications. In several systems, batteries and UCs are integrated using a traditional two-level inverter. In [4], different

ways to integrate battery with UCs for HEV/EV are discussed. In [5], more options to integrate batteries with UCs are presented, such as a multi-port DC-DC converter and a hybrid converter configuration. The system shown in [6] proposes a unique structure to exchange power among battery, UC, and DC loads. In [7], a cascaded multilevel inverter that uses batteries and UCs is proposed as a supporting device for wind power applications. A half-bridge structure is used in this system for batteries, while the system DC bus is composed of UCs via DC-DC converters.

In all the aforementioned systems, battery banks and UC banks are represented as one unit without considering cell-level energy management. However, the series/parallel configuration of energy storage (battery and UC) cells entail higher risks in terms of reliability and safety if an energy management system (EMS) is not present. In addition, factors such as varying internal impedance and self-discharge rates lead to a significant imbalance of cell capacities and operating voltage levels over long periods of use [8-10]. Thus, an EMS is necessary for future electrified transportation systems to manage the cells' energy flow while maintaining their charging/discharging rates within the desirable operating limits.

The ability to develop a power electronic configuration system and an integrated control structure that allows battery/UCs hybridization where each cell or group of cells can be individually managed can significantly benefit the vehicle's performance. Making this system scalable supports system sizing and design as the same structure could be used for different applications and system sizes without system redesign. An effective candidate to achieve this requirement is modular multilevel converters (MMCs) configuration. As indicated in [11], MMCs can generate high voltage with very low levels of total harmonic distortion (THD) while operating at high efficiency due to eliminating the system level inverter and the relatively low switching frequencies of operation. These features make them a suitable candidate for traction applications [12].

Furthermore, the same cascaded structure is used for battery charging as well as load supply. Generally, variations in battery cells' state of charge (SOC) can limit the performance of the whole series string of batteries to the weakest cell [13]. These challenges can easily be negated using MMCs. Active balancing among the cells can be achieved by controlling the various submodules (SMs) to provide the battery system's needed power while maintaining balanced SOC across all battery cells [11, 14]. Finally, the adoption of MMCs in EVs simplifies the integration of UCs into the storage system.

### I.B). Literature Survey on MMCs' Control Algorithms

The use of MMCs presents a control opportunity due to the high number of switching states that grant a higher degree of control freedom. However, developing such a control algorithm is a challenging task as it should simultaneously achieve multiple objectives. These objectives are related to the motor drive output signals (current and voltage), while the rest affect the storage devices' SOC levels and power flow [15, 16].

Managing the operation of batteries and UCs in a hybrid storage system has a noticeable impact on system efficiency and storage devices' lifetime. However, battery and UC cells should operate to maintain uniform degradation across the system components. Since motor drive MMC-based converters need to track multiple control objectives using HSEDs, there is a high degree of freedom to operate the system. This feature disqualifies the use of classical linear control methods to manage the system operation.

In [17], artificial neural networks (ANNs) based management system is used to maintain a similar depleting rate for storage devices. Similarly, in [18], a fuzzy-logic-based approach is presented to manage a battery/UC combination. Due to the complex model of batteries and UCs, heuristic information has been used to drive the controller using several driving patterns.

One of the control techniques that have recently received significant attention for MMCs is model predictive control (MPC). The flexibility in generating the required output voltage/current through a finite number of configurations of the MMC SMs enables specific objectives to be set and optimized. In MPC, different possible switching configurations are simulated to predict the system performance, and the one that yields the optimum performance is then implemented [19]. The objective function is usually taken as a weighted sum of different cost functions [20]. However, as the number of levels increases in MMC, there is a need to reduce the number of configurations considered at any instant by the MPC to maintain a reasonable level of computation complexity.

In [21], the selected objective is to supply the required output current, balance the capacitors' voltages at different levels, and minimize the circulation current. To limit the computation complexity, the authors followed a sequential evaluation procedure. This method is quite effective and practical; however, it imposes a particular priority in meeting the objective function that is not desirable. A similar cost function is considered in [22], where the objective is to develop an MPC method with low computation complexity. First, the optimal number of cells to be turned ON is decided by combining simplified relations for output and circulated currents. Then, the appropriate set of capacitors to be turned ON is then selected following the capacitor voltage sorting. This method is proper when identical capacitors are used at various levels. However, when batteries with different characteristics and UCs are integrated into one system, more elaborate techniques to switch various cells need to be developed. The method in [23] implements MPC based on actual PWM switching to enhance the accuracy in tracking the reference output current. The process selects the next higher and lower levels to the output voltage that optimizes the output current. Each level is activated for a time duration that yields the required average voltage at the inverter output. Despite its accuracy, this approach's computation complexity limits its applicability to a relatively low number of voltage levels. In [24], a method is proposed for three-level inverters to eliminate the need to determine the values of various weighting factors used for the cost function. This method performs effectively for a small number of levels; however, as the number of levels increases, weighting factors need to be included in the cost function.

The advantage of applying MPC for permanent magnet synchronous motor (PMSM) drives is discussed in [25], where a linearized model for the system is used to implement MPC

control. The same objective is addressed in [26] for an interior PMSM. Implementing MPC with permanent magnet motors is proved effective; however, it shall be expanded to MMC systems, as discussed in this paper.

In this paper, the authors propose the use of an MPC algorithm for MP-MMC converters. These converters facilitate the use of HSEDs in EVs in a scalable energy management system (EMS), hereinafter called smart energy management drivetrain system (SEMDS). The proposed system can achieve several control objectives using a one-step horizon MPC while lowering the system size and weight. The proposed MPC algorithm is not unique to the shown configurations. However, it amplifies the benefits of using MP-MMCs.

## II. PROPOSED MP-MMC CONFIGURATIONS

Numerous EMS schemes have been put forward in the literature, and they are categorized as passive and active management based on their balancing mechanism, as shown in Fig. 3. However, passive management is inefficient as significant amounts of energy dissipate in thermal energy via the connected resistors. On the other hand, active management relies on energy sharing; thus, it is more efficient, as shown in Fig. 1.

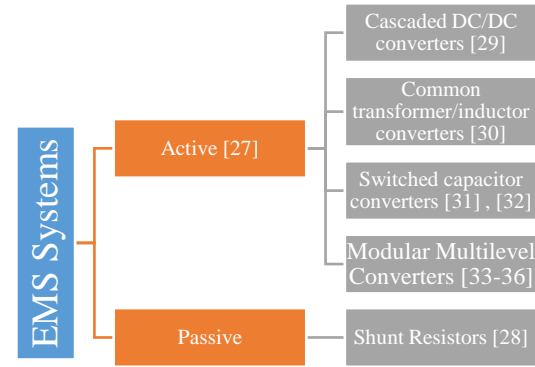


Figure 1. EMS state of the art.

Applying the EMS configurations above into an EV system will process the battery power through dual stages; the EMS and the motor drive system, as shown in Fig. 2, reduce overall system efficiency due to increased conduction losses and increased system weight and size.

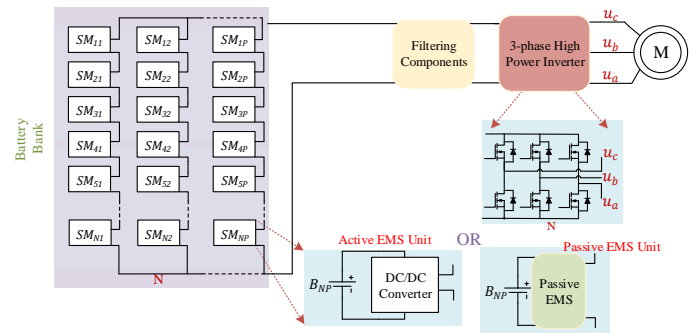


Figure 2. Conventional EV Motor Drive System.

On the other hand, using MMCs in an EMS enables the battery power flow through a single high-frequency power stage, as shown in Fig. 3. The SM modes of operation are shown in the same Fig. Thus, increasing the system efficiency and reducing its size and weight considerably. Additionally, MMCs can operate over a wide range of switching frequencies with low power losses. Furthermore, cascaded MMCs do not rely on capacitors, inductors, or transformers for energy

sharing, signifying compact design. Thus, the modularity of MMCs can be leveraged for use in EVs, where a large number of battery cells are utilized.

The adoption of MMCs in EV systems simplifies the integration of UCs into the storage system. Two different design approaches emerge from exploring the use of MMCs with HESDs. The first approach creates new SMs for every storage (battery or UC) cell/group of cells, increasing SMs and switches in every current path. This configuration is shown in Fig. 4, along with the battery and UC SMs modes of operation.

Alternatively, the second design approach proposed in this paper integrates UC cells into the existing SMs by altering the conventional MMC design by enabling multiple ports (MPs) for every MMC unit, thus, designing MP-MMCs [37]. The latest approach results in lower conduction losses and less switch count. Different possible configurations for an SEMDS using MP-MMCs are shown in Fig. 5.

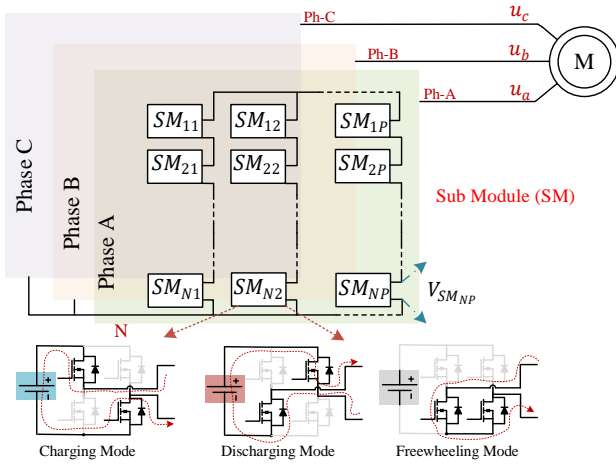


Figure 3. MMC Based EMS and EV Drivetrain configuration.

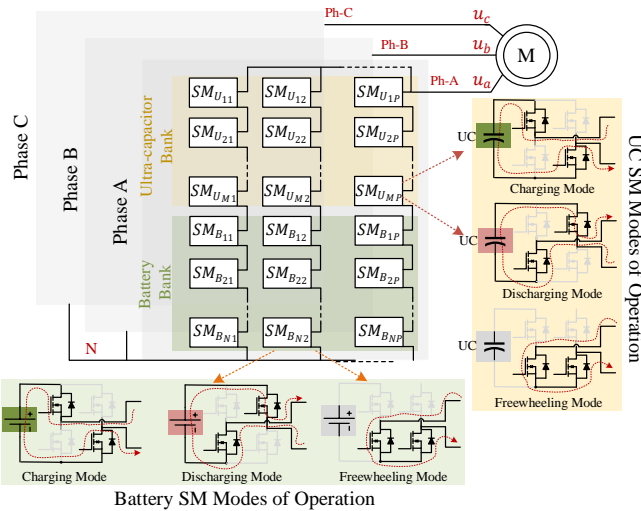


Figure 4. MMC Based EMS for EV Applications using both battery and ultra-capacitor cells.

The configurations shown in Fig. 5 differ from one another in terms of switch count and the voltage stress across switches. The MPC structure proposed in this paper applies to any of the configurations. In this paper, the authors chose MP-MMC option II due to its proximity to the conventional MMC configuration.

There are three defined modes of operation for the shown MP-MMC SM. The first mode of operation is battery only. This mode occurs during low power and below-rated speed

intervals. The second mode of operation is UC only. This mode occurs during the peak power demand intervals in the acceleration and deceleration modes. Finally, the series connection between the battery and the UC cell occurs during the maximum torque per ampere (MTPA) extension interval, as discussed in detail in the next section. An MPC structure manages the power share between the battery and UC cells, as shown in Section III. The modes of operation are shown in and Fig. 6 and Table 1 with their corresponding conduction paths as  $V_B$  is the battery cell voltage, and  $V_{UC}$  is the UC cell voltage.

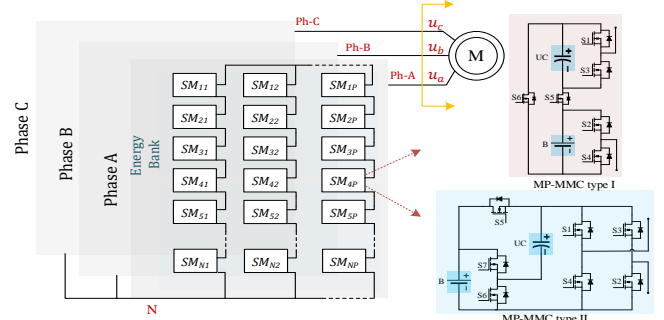


Figure 5. High-efficiency MMC configuration applied for HESD system in EV Applications using both battery and ultra-capacitor cells.

For a given voltage level, three switches are conducting in each of the three modes of operation. Consequently, the reduced number of switches used per SM increases the system efficiency. In comparison, in a conventional hybrid system with a single battery cell or a UC cell for each H-bridge module, a minimum of four switches are conducted to establish a series path between two modules.

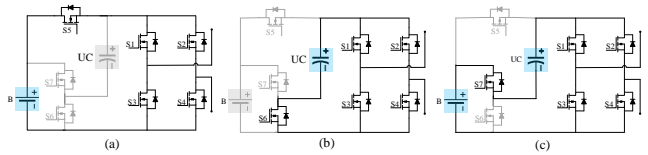


Figure 6. MP-MMC SM modes of operation a) battery only, b) UC only, and c) battery and UC in series.

Table 1. Sub-module Converters Switching States

	S1	S2	S3	S4	S5	S6	S7	Output
Battery Low Power Mode	1	0	0	1	0	0	1	$V_B$
	1	1	0	0	0	0	1	0
	0	1	1	0	0	0	1	$-V_B$
UC High Power Mode	1	0	0	1	0	1	0	$V_{UC}$
	1	1	0	0	0	1	0	0
	0	1	1	0	0	1	0	$-V_{UC}$
Battery + UC MTPA Extension	1	0	0	1	1	0	0	$V_B + V_{UC}$
	1	1	0	0	1	0	0	0
	0	1	1	0	1	0	0	$-V_B - V_{UC}$

Once the SM DC source is selected based on the mode of operation, the H-bridge inverters are switched using a pulse width modulation (PWM) scheme with a multi-carrier technique called Phase Disposition PWM (PDPWM), as shown in Fig. 8 [38]. High-frequency carrier signals are stacked above and below the zero reference with a  $0^\circ$  phase shift. For  $n$  levels in the output waveform,  $n - 1$  carrier signals are used. The carrier signals are assigned to different SMs based on their SOC levels, as shown in Fig. 7.

The proposed configuration stems from the single star MMC (SSMMC) architecture. Thus, this configuration inherits SSMMC features, such as low cell count and practicability [39]. Unlike single delta and double star configurations, SSMMC configurations do not suffer from circulating current

between their phases. However, a negligible amount of circulating current can be observed between the arms of the same phase. Therefore, the authors used the motor voltage reference as the primary commanding signal that decides the number of activated cells to eliminate this problem. This number will be universal among all arms. Thus, arms' voltage levels stay within close proximity to one another. Thus, eliminating any circulating current between the battery cells. The use of circulating current to balance the storage cells' SOC had been discussed in the literature. However, in this paper, the authors balance the SOC of the storage cells using the supplied motor current. This capability further increases the system's efficiency. Additionally, the proposed configuration eliminates the use of balancing capacitors, as the arm voltages are directly supplied from the battery cells.

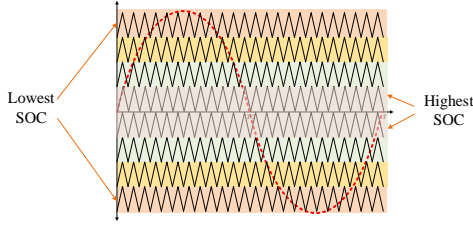


Figure 7. Carrier cascaded PWM technique for EMS applications during the discharging cycle.

Additionally, the common-mode voltage of this configuration is much lower than that of the conventional motor drive system shown in Fig. 2 due to the inherently lower  $dV/dT$  [40] caused by designing the control algorithm to only switch ON or OFF one SM in every switching cycle. As more SMs are used in the system,  $dV/dT$  is lower, and thus, the common-mode voltage will be negligible. In this paper, the absence of common-mode voltage was evident in both simulations and experimental results, as seen in Section VI.

### III. BATTERY MODELING AND SOC ESTIMATION

SOC Model-based estimation (MBE) is a well-established control technique that requires a dynamic model of the system. This model estimates the system's current state and predicts changes in the system state and system outputs given an input vector. Once the output is predicted, measurement of actual output is made and compared against the prediction, and the estimation is adjusted accordingly. Thus, MBE is a closed-loop system, giving it a method of accounting for real sources of error.

#### A. Li-ion battery modeling

The externally measurable electrical dynamics of Li-ion battery behavior can be modeled using an equivalent circuit model such as that shown in Fig. 8 [41-43].

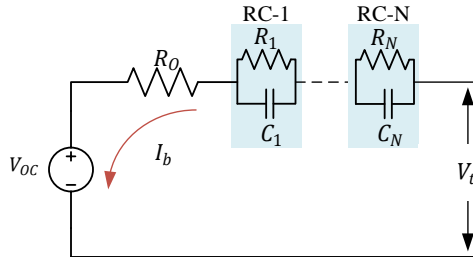


Figure 8. Equivalent circuit model used for the Li-ion battery cells.

The voltage source in the model represents the open-circuit voltage (OCV) of the battery. This voltage is dependent on

battery SOC. The relationship between  $V_{OC}$  and SOC is unique for every battery type. Thus, battery testing is required to generate this relationship.

The resistor  $R_0$ , represents the internal resistance of the cell. This resistance is caused by limited chemical kinetics during the charge and discharge process and exhibits an SOC and temperature dependence. The resistor-capacitor pair represents the diffusion voltage of the cell. A model may include more than one RC pair to match observed dynamic behavior as needed.

#### B. Li-ion battery SOC estimation

In this paper, the authors present the integration of Li-ion battery cells' SOC estimation into the proposed system using Kalman filtering. A Kalman filter is a recursive linear quadratic estimator that provides the optimal state estimate of a linear dynamic system under the influence of white Gaussian noise. The general expressions for the six-step Kalman filter can be expressed as in table 2.

Consequently, Eqns. 1 and 2 show the general form of the discrete-time state-space model of a linear dynamic system under the influence of white noise disturbances, which corresponds to the general form given by the used battery model with added noise vectors. Here  $x_k$  is the state vector,  $u_k$  is the system input vector,  $y_k$  is the output vector,  $w_k$  represents the process noise vector, and  $v_k$  represents the sensor noise vector. It is assumed that  $w_k$  and  $v_k$  are uncorrelated with each other and the state vector, and they are typically distributed random variables with zero means.

Table 2 Prediction and correction steps for the Kalman filtering used in estimating Li-ion battery cells' SOC levels.

Prediction phase	
Step 1	Predict the current state of the system, given all previous output observations. $\hat{x}_k^- = E[x_k   Y_{k-1}] = A_{k-1} \hat{x}_{k-1}^+ + B_{k-1} u_{k-1}$
Step 2	Compute the covariance of the error between the state and the prediction. $\begin{aligned} \sum \tilde{x}_k^- &= E[(x_k - \hat{x}_k^-)(x_k - \hat{x}_k^-)^T] \\ &= A_{k-1} \sum \tilde{x}_{k-1}^+ A_{k-1}^T + \sum \tilde{w}_k \end{aligned}$
Step 3	Measure system input and predict the system output given all previous output observations. $\hat{y}_k^- = E[y_k   Y_{k-1}] = C_k \hat{x}_k^- + D_k u_k$
Correction Phase	
Step 4	Measure system output and compute the Kalman gain matrix using state prediction and output prediction errors. $\begin{aligned} L_k &= \sum \tilde{x}_k^- \tilde{y}_k (\sum \tilde{y}_k)^{-1} \\ &= \sum \tilde{x}_k^- C_k^T [C_k \sum \tilde{x}_k^- C_k^T + \sum \tilde{v}_k]^{-1} \end{aligned}$
Step 5	Compute the state prediction correction using the Kalman gain matrix. $\hat{x}_k^+ = \hat{x}_k^- + L_k \tilde{y}_k$
Step 6	Compute the error covariance of the updated prediction. $\sum \tilde{x}_k^+ = \sum \tilde{x}_k^- - L_k \sum \tilde{y}_k L_k^T$



By substituting (1) and (2) into the general expressions of the linear Kalman filter algorithm shown in table 2, the recursive, six-step SOC state estimation algorithm is derived.

$$x_{k+1} = A_k x_k + B_k u_k + w_k \quad (1)$$

$$y_k = C_k x_k + D_k u_k + v_k \quad (2)$$

An MBE approach using Kalman filtering shown in Fig. 9 (where  $I_b$  is the battery cell current, and  $V_t$  is the battery cell terminal voltage) uses all available battery data to make predictions since both current and voltage sensors are employed for every battery cell in the proposed configuration. As shown, the process is broken down into a prediction phase and a correction phase. In the prediction phase, the load current is sampled at time  $k$  and fed in parallel to the battery model. The battery model propagates the previous state estimate,  $\hat{x}_{k-1}^+$  and current  $u_k$  through the system and outputs a prediction of the terminal voltage  $\hat{y}_k$  and an estimated state  $\hat{x}_k^-$ . In the correction phase, the terminal voltage of the battery,  $y_k$  is sampled at time  $k$  and compared with the model prediction  $\hat{y}_k$ . A correction is then applied to the state estimation  $\hat{x}_k^-$  which is proportional to the error between the model prediction and the measured voltage to produce a corrected state estimate  $\hat{x}_k^+$ . Not shown in the block diagram is the computation of the Kalman gain, which is the gain factor,  $L_k$ , which scales the prediction error in the state estimate correction. The gain is computed using the covariance matrices of the state and output equations. Thus, high certainty in the estimate and low certainty in the output results in a smaller gain, while low certainty in the estimate and high certainty in the output results in a larger gain.

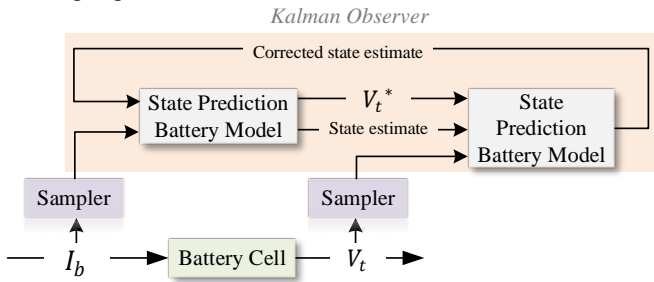


Figure 9 Block diagram of the SOC estimation process.

For the prediction phase to generate accurate predictions with low error, the equivalent circuit battery model must be parameterized appropriately. Therefore, two testing procedures were developed to parameterize and validate model performance, as shown in the validation results section.

#### IV. MOTOR REFERENCE GENERATION

##### A. Machine model

An accurate mathematical model of the machine is necessary to implement the model predictive control strategy to the IPM. The mathematical model of IPM is given in [38] as:

$$V(t) = L \frac{di(t)}{dt} + Ri(t) + e(t) \quad (3)$$

where  $V(t)$  is the phase voltage,  $i(t)$  is the phase current,  $L$  is the coil inductance,  $R$  is the resistance of the winding, and  $e(t)$  is the back emf. The rotor of the IPM motors have magnetic saliency, and the inductance measurement results will change according to the rotor position (i.e.  $L_d \neq L_q$ ). The effective inductance of the IPM machine is given by  $L_{IPM}$

$$L_{IPM} = \frac{3}{2} \left( \frac{L_q + L_d}{2} - \frac{L_q - L_d}{2} \cos 2\theta \right) \quad (4)$$

where  $L_d$  and  $L_q$  are the motor d and q inductances, respectively, while  $\theta$  is the rotor position.

After rearranging and discretizing Eqn. 1, future values of load current,  $i(k+1)$ , can be predicted from voltages and measured currents at the  $k^{th}$  sample as shown in (5)

$$i(k+1) = i(k) \left( 1 - \frac{T_s R}{L_{IPM}} \right) + \frac{T_s}{L_{IPM}} (V(k) - e(k)) \quad (5)$$

where,

$$e(k) \approx V(k-1) - \frac{L_{IPM}}{T_s} i(k) - \left( R - \frac{L_{IPM}}{T_s} \right) i(k-1) \quad (6)$$

##### B. Reference generation by MTPA and FW algorithms

When the motor speed is below the rated speed, the reference current is generated using the MTPA algorithm. For speed values higher than the rated speed, the Maximum torque output can be generated only when the motor operates in the field-weakening (FW) region.

The well-known voltage and torque equations describing the electrical characteristics of an IPM motor are:

$$V_d = Ri_d + L_d \frac{di_d}{dt} - \omega L_q i_q \quad (7)$$

$$V_q = Ri_q + L_q \frac{di_q}{dt} + \omega (L_d i_d + \lambda) \quad (8)$$

$$T_e = \frac{3P}{2} [\lambda i_q + (L_d - L_q)(i_d i_q)] \quad (9)$$

It is seen from Eqn. 9 that if the  $dq$  inductance values are not identical, torque is generated when the magnitude of the  $d$  axis current is increased. Therefore, minimizing the total stator current helps decrease the system conduction losses, thus increasing the performance efficiency at various loading conditions. This operational mode is referred to as the MTPA mode.

Considering the equation below describing the maximum voltage magnitude  $V_{sm}$  that can be applied to the motor windings by the three-phase inverter [44, 45]:

$$V_d^2 + V_q^2 \leq V_{sm}^2 \quad (10)$$

Assuming that the voltage drop across the winding resistance is small and substituting the machine voltage equations at steady state into (10):

$$\frac{(i_q)^2}{L_q^2} + \frac{\left(i_d + \frac{\lambda}{L_q}\right)^2}{L_d^2} \leq \left(\frac{V_{sm}}{\omega}\right)^2 \quad (11)$$

It can be seen from the preceding equations that the  $dq$  current selection is not only limited by the stator current magnitude but also by the maximum stator voltage magnitude. While the limit on the stator current magnitude is a constant circle in the DQ current plane, the voltage limit is an ellipse that shrinks as the motor speed increases. When the point corresponding to the commanded torque on the MTPA curve is no longer inside the voltage limit ellipse, the motor must operate in FW mode. Operation in the FW mode allows high motor speeds to be achieved at the cost of lower motor torque.

Analytical expressions of the MTPA curve found in [38, 46] produce the following:

$$i_q = \sqrt{\frac{\lambda}{(L_d - L_q)}} i_d + i_d^2 \quad (12)$$

$$i_d = \frac{\sqrt{4(L_d - L_q)^2 i_q^2 + \lambda^2} - \lambda}{2(L_d - L_q)} \quad (13)$$

As the motor speed exceeds the MTPA curve's limits, the controller tracks FW along the constant torque curve. Further, as the commanded torque is no longer valid at any speed, the controller follows the maximum torque per voltage curve.

### C. Extended MTPA region

In this paper, the employed EMS can generate different voltage levels to the EV motor to extend the MTPA region, increasing the system efficiency and reducing the emitted heat resulting from conduction losses. This is achieved by selecting the number of SMs that will contribute to the motor's voltage. At low speeds, lower voltage is applied to reduce the system switching losses, and as the motor speed increases, more SMs contribute to the voltage to extend the MTPA region. Furthermore, operating the UCs in series with the battery cells increases the motor phase voltages at high operational speeds. The impact of extending the MTPA region is shown in Fig. 10.

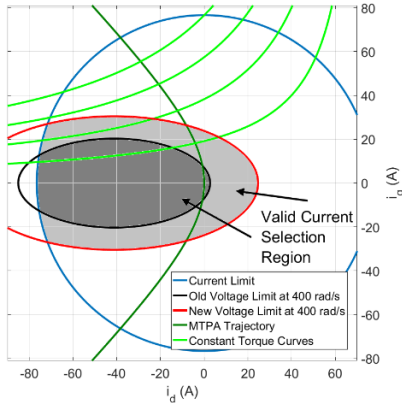


Figure 10. Impact of the MTPA extension on EV IPM motor regions of operation.

## V. MP-MMC CONTROL

### A. Switch matrix

In the proposed topology, the MP-MMC SM is composed of seven switches; four switches ( $S_1 - S_4$ ) for the SM H-bridge and three switches ( $S_5 - S_7$ ) for the battery/UC selection configuration, as shown in Fig. 6. Tables 3 and 4 show the operational effect of every switch on the SM voltage where  $V_{SM}$  is the SM output voltage magnitude,  $V_{Battery}$  is a battery cell terminal voltage, and  $V_{UC}$  is the UC cell terminal voltage.

The switching of an MMC, composed of  $k$  series strings and  $n$  SMs in every string, is expressed in a switch matrix ( $SW_{matrix}$ ) shown below:

$$SW_{matrix} = \begin{bmatrix} SW_1 \\ SW_2 \end{bmatrix} \quad (14)$$

$$SW_1 = \begin{bmatrix} S_{k11} & S_{k21} & \dots & \dots & \dots & S_{k(n-1)1} & S_{kn1} \\ S_{k12} & S_{k22} & \dots & \dots & \dots & S_{k(n-1)2} & S_{kn2} \\ S_{k13} & S_{k23} & \dots & \dots & \dots & S_{k(n-1)3} & S_{kn3} \\ S_{k14} & S_{k24} & \dots & \dots & \dots & S_{k(n-1)4} & S_{kn4} \end{bmatrix}_{4 \times n} \quad (15)$$

$$SW_2 = \begin{bmatrix} S_{k15} & S_{k25} & \dots & \dots & \dots & S_{k(n-1)5} & S_{kn5} \\ S_{k16} & S_{k26} & \dots & \dots & \dots & S_{k(n-1)6} & S_{kn6} \\ S_{k17} & S_{k27} & \dots & \dots & \dots & S_{k(n-1)7} & S_{kn7} \end{bmatrix}_{3 \times n} \quad (16)$$

Table 3. Switching sequence of switches ( $S_{1-4}$ )

SM output voltage	$S_{kn1}$	$S_{kn2}$	$S_{kn3}$	$S_{kn4}$
$+V_{SM}$	1	1	0	0
$-V_{SM}$	0	0	1	1
0	1	0	1	0

Table 4. Switching sequence of switches ( $S_{5-7}$ )

$S_{kn5}$	$S_{kn6}$	$S_{kn7}$	$ V_{SM} $	HESD Combination
1	0	0	$V_{Battery}$	Battery
0	1	0	$V_{UC}$	UC
0	0	1	$V_{UC+Battery}$	Battery + UC
0	0	0	0	None

$SW_{matrix}$  is composed of two submatrices,  $SW_1$  and  $SW_2$ .  $SW_1$  is the H-Bridge matrix that controls the direction of the current. Each column of  $SW_1$  corresponds to four switches of the H-bridge inverter in a given SM,  $S_{pni}$  represents the ON/OFF state of each switch in the form of 0 (OFF) and 1 (ON).  $SW_2$  is the HESDs matrix. Each column of the switch matrix  $SW_2$  corresponds to three switches whose operation determines the HESDs used from the given SM. After each sample time ( $T_s$ ), the switch matrix is updated and sent to the respective gate drivers controlling the switching devices.

### B. The voltage output from each submodule

Inherent to the H-Bridge topology, each submodule can generate positive, negative, and zero voltage. Thus, seven different voltage levels can be generated from a single submodule, as shown in Eqn. 17

$$V_{SM} = \begin{cases} 0 \\ V_{battery} \\ V_{UC} \\ V_{battery} + V_{UC} \\ -V_{battery} \\ -V_{UC} \\ -(V_{battery} + V_{UC}) \end{cases} \quad (17)$$

The output voltage of an MP-MMC can be expressed as a function of the switch matrix ( $SW_{matrix}$ ) as given below:

$$M = [1 \ 0 \ -1 \ 0] \quad (18)$$

$$V_{SMn} = |M \cdot SW_1(:, n)| \cdot |V_{battery} \ V_{UC}| [SW_2(:, n)] \quad (19)$$

$$V_o = [V_{SM1} \ V_{SM2} \ V_{SM3} \ \dots \ V_{SMn}] \quad (20)$$

$$V_{MMC} = \sum_{i=1}^n V_{SMi} \quad (21)$$

Matrix  $M$  is selected such that its product by any column of  $SW_1$  will layout the voltage polarity of the given SM. The voltage of each submodule in the MMC is presented in Eqn. 19 as it is composed of two parts, the product  $|M \cdot SW_1(:, n)|$

that provides information on the SM voltage polarity and  $|[V_{battery} \ V_{UC}][SW_2(:,n)]|$  that is responsible for managing the energy between the SM HESDs. The output voltage of an MMC is the sum of all the SMs voltage as shown in Eqn. 21.

### C. Application of MPC

The SEMDS feeds the IPM motor, as shown in Fig. 5. The proposed control system for speed control of an IPM motor is shown in Fig. 11 [47]. An MPC is used to control the motor speed by tracking the reference phase current values. A discretized model of an IPM motor is used to predict the future states of the motor. A cost function optimizes the voltage state used for the reference current track. The error between the reference speed ( $\omega^*$ ) and the actual speed ( $\omega$ ) of the motor is used to generate commanded torque ( $T_e$ ). The commanded torque signal is converted to the reference current ( $i_{abc}^*$ ) using MTPA, extended MTPA, and FW algorithms. The reference current generation block provides the UC percentage that should be used in the MPC algorithm. The MPC block predicts the current future states and optimizes the cost function from  $14n + 7$  available SOC selections of battery and UC cells where the number of SMs in a string is  $n$ . Once the optimized voltage is found, the controller selects the best combination of battery and UC cells based on their SOC values and the percentage share given by the MTPA/extended MTPA and FW algorithms. The MPC algorithm then generates the switching matrix to supply the required three-phase power to the IPM motor. The Pseudocode used to create the switch matrix ( $SW_M$ ) is shown in the Appendix of this paper.

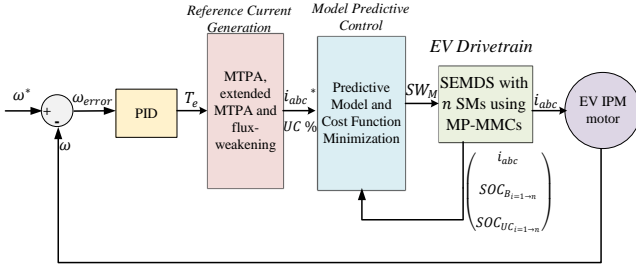


Figure 11. MPC structure applied to MP-MMCs for an EV drivetrain.

The cost function is the principle distinction among MPC and other predictive control procedures. In this paper, the quality of speed tracking is dependent on the quality of the reference current track. Therefore, the main component of the cost function is an error term between the reference current and its predicted value.

$$J = |I_{ref} - I(k+1)| \quad (22)$$

The constraints are added to the cost function with their weighting factors to allow for a tradeoff level between the function terms. However, on adding the additional terms to the cost function, the main terms' influence reduces and, therefore, an optimization process is used to find the optimal solution. The constraints added in the proposed system are:

#### a) Voltage ripple minimization

The rate of change in the phase voltage needs is limited to reduce  $dv/dt$ . To implement the minimization of voltage ripple,  $|v(k+1) - v(k)|$  is added to the cost function. It is the difference between the measured value of the voltage at the  $k^{th}$  state and the  $k+1^{th}$  state. The general form of adding this constraint is with a weighing factor  $\lambda_2$

#### b) Switching frequency minimization

For accurately tracking the reference current, the switch matrix changes every sample time. However, when the tracking error is within a given bound, the number of switching states that change at each sampling time is minimized by a factor ( $f$ ) is the cost function to reduce the switching losses where  $f$  is the number of switches that change their state on applying a new switching matrix.

$$f = \sum_{i=1}^N |SW_{matrix}(k+1) - SW_{matrix}(k)| \quad (23)$$

where  $N$  is the total number of elements in the switch matrix.

#### c) Limits to phase current and phase voltage

The EV drivetrain components (motor windings, Mosfets, etc...) are limited in their current tolerance. Thus, a nonlinear term is added to the cost function to enforce the system operating within its limits. On crossing the boundaries of current tolerance, the function,  $F_{lim}(i^p)$  increases the value of the cost function to a very high value leading to a rejection of that switching state. Thus, the mathematical expression of the function is:

$$F_{lim}(i^p) = \begin{cases} \infty, & \text{if } |i^p| > I_{max} \\ 0, & \text{if } |i^p| < I_{max} \end{cases} \quad (24)$$

At every instant, the MPC evaluates the cost function ( $14n + 7$ ) times. Thus, the scheme is highly calculation-intensive. To reduce the amount of computation, speed up the voltage selection decision, and reduced  $dv/dt$  The cost function is dependent on the tracking error bound as explained below:

**Low Error Mode:** If the error between the reference current and the actual current at instant  $k$ , is below an allowed limit  $E_l$ , and  $I(k+1) < I_{max}$ , the previous voltage selection is retained without reevaluating the cost function again.

$$|I_{ref} - I(k)| < E_l \quad (25)$$

**Within The Error Bound:** If the tracking error lies between the error bounds, the following cost function is used

$$J = \lambda_1 |I_{ref} - I(k+1)|^2 + \lambda_2 |V(k) - V(k+1)| + \lambda_3 f + F_{lim} \quad (26)$$

where  $\lambda_1, \lambda_2$  and  $\lambda_3$  are weighting coefficients. The effect of weighting factors is shown in Fig. 12 using 50 SMs. The first term in the cost function penalizes the current tracking error, the second term minimizes the voltage ripple, and the third term reduces the switching frequency.

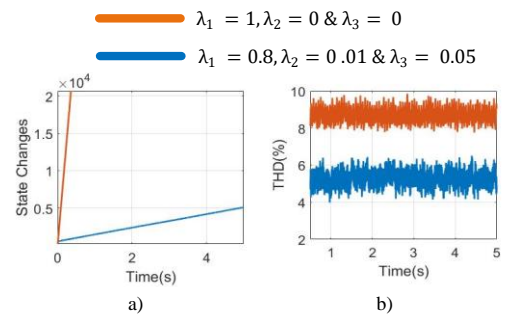


Figure 12. (a) Number of voltage state changes & (b) Total harmonic distortion %

**High Error Mode:** If the reference tracking error goes above a maximum allowed error bound, the cost function is shown in Eqn. 27 is evaluated

$$J = |I_{ref} - I(k+1)|^2 + F_{lim} \quad (27)$$

Another objective of the SEMDS is to balance the SOC levels of all battery and UC cells. Using the terminal voltage SOC estimation [43], the MPC balances the storage cells' voltage levels. Each cell has a different rate of discharge due to the difference in electrochemical characteristics. There is a need to incorporate a voltage balancing algorithm in the MPC algorithm to ensure all storage cells at the same terminal voltage. The algorithm gives priority to the reference track first, followed by voltage balancing. The principal is to lower the use of Low voltage cells ( $C_{LV}$ ) in comparison to cells with high voltage ( $C_{HV}$ ) to ensure the rate of voltage drop is less in  $C_{LV}$ . The results of balancing 10 UC cells using the MPC algorithm are shown in Fig. 13 to verify SOC balancing system effectiveness. It is clear from the results that the SOC of the UC cells balanced by the end of the short driving cycle even though the UC cells started the cycle with different terminal voltage levels.

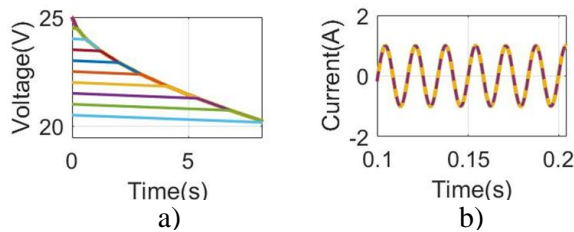


Figure 13. State of Charge equalization: a) Terminal voltage balance during ten cell Modules discharge with different initial Voltages. b) Tracking of the reference current

## VI. SYSTEM VALIDATION RESULTS

### VI.A). Battery SOC estimation and testing

As explained in Section III, an equivalent circuit model for the battery is built, and an SOC estimations algorithm is followed. The authors then present the battery experimental testing results using a pulse discharge test (PDT) and Urban Dynamometer Driving Schedule (UDDS) current signal.

The PDT is designed to extract all parameter values (SOC vs. OCV relationship, R, and C values). The pulse discharge load profile consisted of 30 discharge pulses intended to decrease the battery SOC by 3.33% relative to its nominal capacity, with a sample rate of 1Hz and a cutoff voltage of 9V. Each discharge was performed at a constant 1C (5A) discharge rate for 120 seconds, followed by a resting period of 780 seconds for a total period pulse discharge of 900 seconds (15 minutes) at a duty cycle of 0.133. The 1C discharge rate was chosen to align test results with the manufacturer's reported nominal capacity, which is defined by the mean battery capacity when discharged at a constant rate of 1C. This allows the pulse discharge test to be used to determine the battery's actual capacity, Q, which is a vital battery parameter for determining the state of charge, under a well-defined criterion. The 3.33% increment in SOC was chosen to balance the need for sufficiently high resolution of parameter vs. SOC variation against testing time and model complexity. The resting period was selected to allow the cells to approach an equilibrium condition after each discharge, thereby allowing the terminal voltage to approach OCV for the given SOC. The low discharge rate also allows for a smaller resting period since the cell approaches its equilibrium condition quickly. The

estimated battery terminal voltage and the experimentally measured one under the PDT test are shown in Fig. 14.

A preliminary investigation of the data was performed to determine the optimal number of RC pairs necessary to represent the observed cell behavior adequately. Based on this analysis, it was determined that two RC pairs were sufficient for describing the cell behavior adequately and without adding unnecessary complexity.

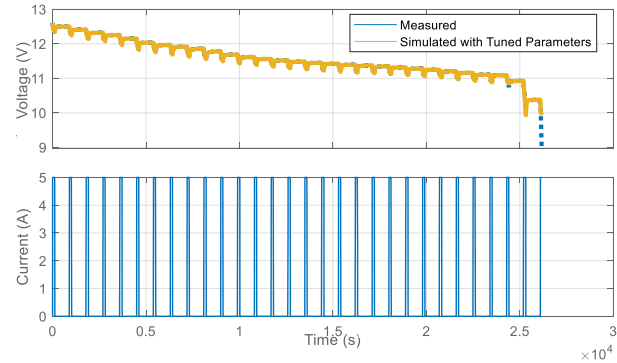


Figure 14. Experimentally measured vs. simulated battery terminal voltage under the PDT.

The second test was devised using the US EPA's UDDS to serve as a basis for evaluating the accuracy of the battery model post-parameterization. The UDDS cycle provides a more dynamic load environment comparable to the intended use-case of the battery storage cell in the system. Therefore, the UDDS cycle was repeated until the battery terminal voltage reached 9V. The estimated battery terminal voltage and the experimentally measured one under the UDDS test are shown in Fig. 15.

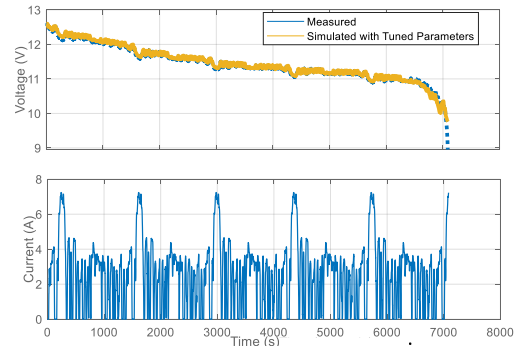


Figure 15. Experimentally measured vs. simulated battery terminal voltage under the PDT.

Finally, the SOC estimation algorithm performance is shown in Figure 16. The average confidence interval over the entire range of SOC for the UDDS test cycle was 2.23%, indicating that, on average, the state estimate produced by the piecewise linear Kalman filter will be within  $\pm 2.23\%$  of the actual value with a 99.7% confidence. The actual SOC, which was used to determine the error and gauge the estimator performance, was calculated by coulomb counting the input current during the controlled environment of the test cycle.

### VI.B). MP-MMC system performance

The proposed control scheme's performance has been tested through a downsized experimental validation, hardware in the loop (HIL), and co-simulations using Matlab/Simulink with PSpice models. The system's experimental prototype using four SMs of MP-MMCs along with battery cells, UC cells, an



electronic load, and a Texas Instruments TMS320F28377D is shown in Fig. 17.

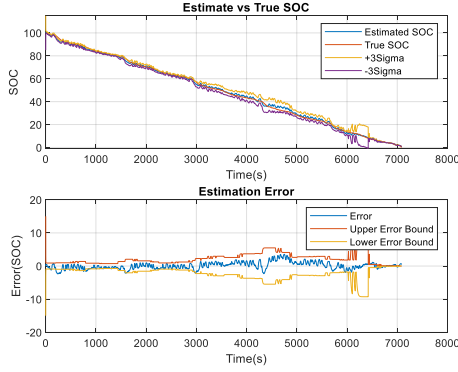


Figure 16. SOC estimation algorithm performance under the UDDS test.

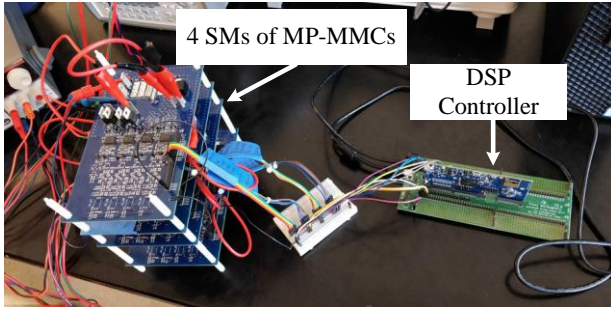


Figure 17. Four MP-MMC SMs' prototype developed and used for testing.

The voltage waveforms of the developed system using the four SMs in battery-only mode, where each battery terminal voltage is rated at 12 v are shown in Fig. 18. In comparison, the voltage and the current waveforms of the load for three SMs at the same rated voltage for UC-only mode are shown in Fig. 19. Table 5 is provided to validate the system's ability to balance the SOC of the connected storage cells. This table shows the SOC decrease for every battery cell while applying the proposed MPC system. In this case study, the four cells started at slightly different SOC levels and ended up with the same final SOC without any external balancing circuitry.

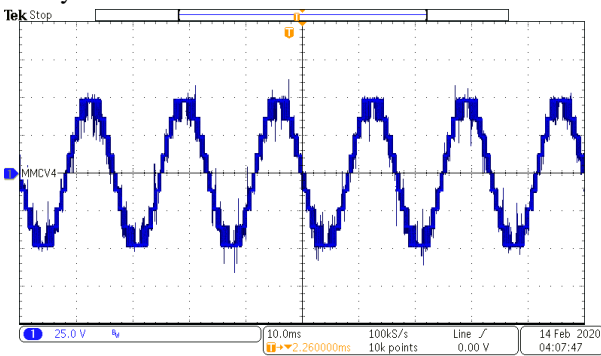


Figure 18. 9 Level voltage output for the SMEDS using 4 SMs (each SM represents a battery cell rated at 12 v).

The system is then examined under a UDDS driving cycle to test its transient and steady-state performance, the power-sharing between HESDs, and the extension of the MTPA region of operation for the used IPM motor. The system parameters used for testing are shown in tables 6 and 7.

Reference currents are generated using a current controller, which adheres to MTPA, MTPA extension, and FW control.

The testing results reveal the performance of the MP-MMCs in realistic motor loading. Only the first 315 s of the UDDS drive cycle were used for testing purposes. The reference current generator output produced the  $d$  &  $q$  output currents and the percentage of UC cells needed to support the D.C. bus (for extending the MTPA region) and supporting high power loads. The system was successfully tracking the vehicle reference speed, as shown in Fig. 20.

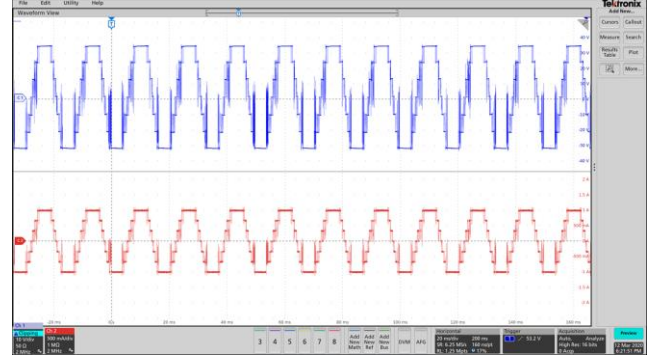


Figure 19. 7 level voltage and current waveforms for the SMEDS (each SM represents a UC cell rated at 12 v).

Table 5. Experimental SOC balancing for 4 battery cells using the proposed MPC system.

Battery Cell initial SOC	Discharging time at 0.5C	SOC Decrease	Final SOC
82%	10 minutes	4.7%	77.3%
82.4%		5.1%	
82.8%		5.5%	
83.2%		5.9%	

TABLE 6. MOTOR PARAMETERS

$L_d$	$L_q$	$\lambda$
1.59 MH	2.05MH	0.175WB

TABLE 7. VEHICLE PARAMETERS

$m_{EV}$	$C_0$	$C_d$	$GR$
1360kg	0.0011	0.26	5

The reference current generation block provides the percentage of UC cells that must be used to provide the extended MTPA range or support large current transients, as shown in Fig. 21. It is clear from the presented results that the UC supports two different modes of operation. The first mode is the MTPA extension shown in Fig. 21. As the motor speed increases beyond the limitations of the bus voltage provided by the battery cells. The second mode is the high power transients that frequently occur during acceleration and deceleration periods.

The  $dq$  axes voltage and current magnitudes of the motor windings and the motor speed and torque are shown in Fig. 22. Finally, the phase to phase voltages generated by the MPC for a selected region are demonstrated in Fig. 23 using 100 SMs.

Finally, a short time scale results are used for a 100 SM system using HIL (OPAL-RT 4200) in Fig. 24 while applying the proposed MPC system. In these results, after the motor achieves the reference rotor speed of 100 rad/s with a 350 Nm load, the load is dropped from 350 Nm to 50 Nm. The transient

results show the system's quick recovery to generate the required sinusoidal voltage and current signals.

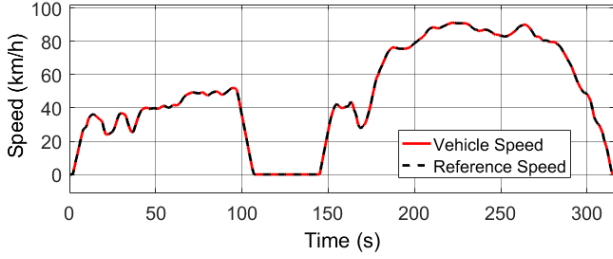


Figure 20. The vehicle speed tracks the reference speed with extreme accuracy.

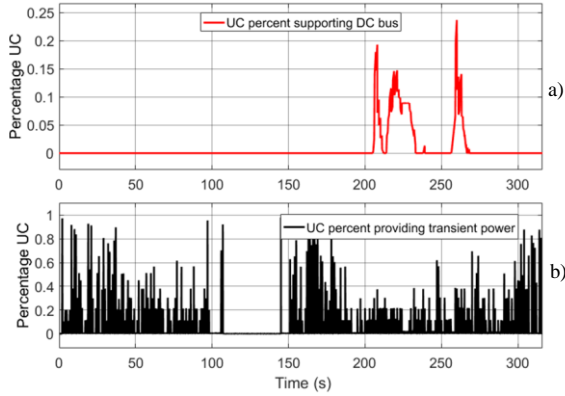


Figure 21. a) The percentage of UC cells needed to support the DC bus as the motor speed exceeds the rated speed. b) The percentage of UC cells needed to absorb or inject high-power transients.

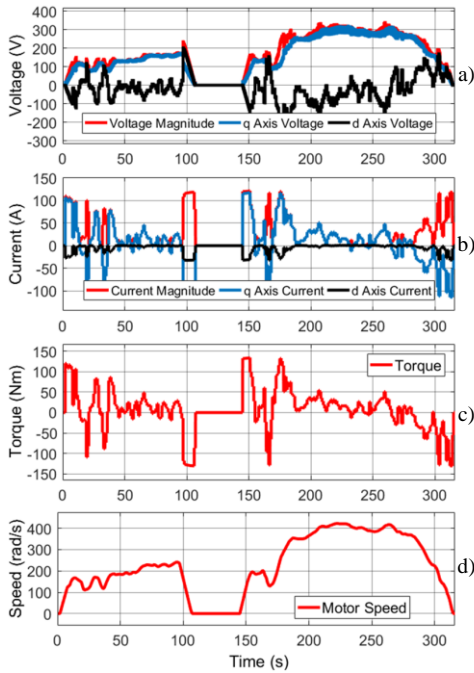


Figure 22. The motor a) DQ axes voltage magnitude, b) DQ axes current magnitude, c) operating torque, and d) operating speed.

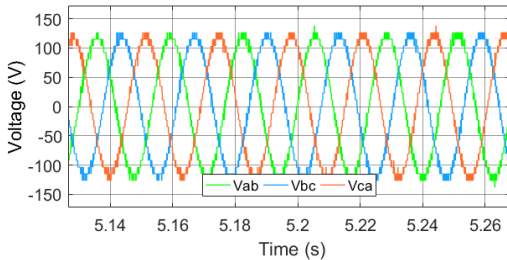


Figure 23. phase-to-phase voltages across the motor using 100 SMs

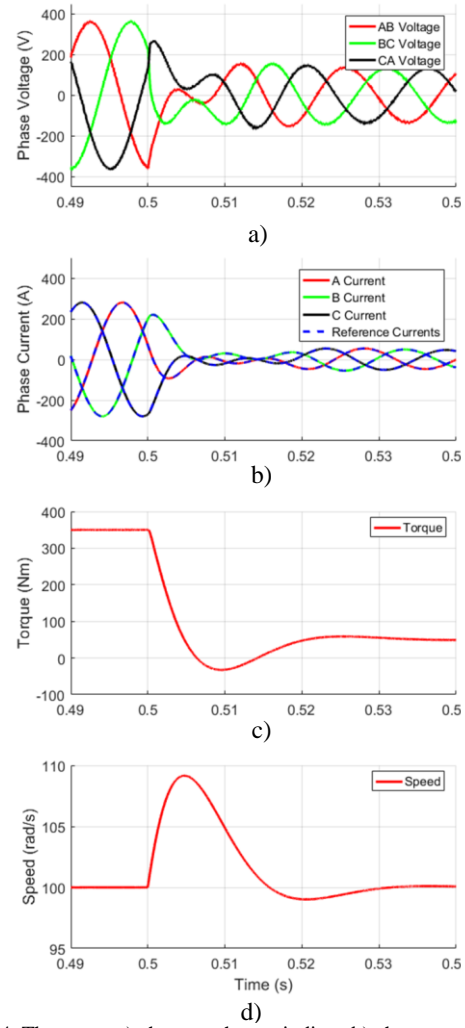


Figure 24. The motor a) phase to phase windings b) phase currents and reference currents, c) operating torque, and d) operating speed. The motor speed is regulated at 100 rad/s. The load torque drops from 350Nm to 50Nm.

## VII. CONCLUSION

The proposed MP-MMC-based configuration enables the seamless integration of UC cells into an EV drivetrain. The designed system successfully increased the EV drivetrain performance by shielding the battery cells from high power pulses, balancing the SOC of the system storage cells, and extending the operation's MTPA region. Furthermore, an MPC scheme with a one-step prediction horizon is proposed to control the SMs of the MP-MMCs in driving an IPM EV motor. The developed MPC algorithm tracks the current motor error while reducing the system switching frequency and the output voltage ripple. In addition, the algorithm is reactive to the system monitoring error. This feature decreased the computational algorithm intensity. Finally, a downsized prototype is built along with co-simulations and an HIL system for testing purposes. The test results validated the developed EV drivetrain and verified its effectiveness in driving an EV under various operating conditions and real driving cycles.

## APPENDIX

Pseudocode of generating the switch matrix ( $SW_M$ ) is provided in this Appendix. The code is provided for a case study of generating an output voltage of 50 V, under the assumption of a battery and a UC cell voltage level of 10 V per cell for simplification. The code steps and necessary equations are shown in table 7 below.

<b>Step 1</b>	<b>MPC decides the magnitude and polarity of the voltage required,</b> $V_{req} = +50 \text{ v}$	<b>Step 7</b>	Matrix UCO is created, which contains the switching stated for SM, which needs to turn on only UCs $UCO = B' - C$ $UCO = [SW(:,2)]$ $If V_{req} > 0$ $n = 1: order(UCO)$ $UCO(n) = [1 \ 0 \ 0 \ 1 \ 0 \ 1 \ 0]$ $n = n + 1$ $else$ $n = 1: orcer(UCO)$ $UCO(n) = [1 \ 0 \ 0 \ 1 \ 0 \ 1 \ 0]$ $n = n + 1$ $End$
<b>Step 2</b>	MTPA, MTPV, and FW algorithms decide the % share of the UC and Batteries for producing the required voltage. Assume three battery cells and 2 UC cells.		
<b>Step 3</b>	Each column of the switching matrix tells whether a submodule is on/off and what combination of UC and Battery is being used in each submodule. $SW_{matrix}(k) = \begin{bmatrix} SW11 & SW21 & \dots & SWn1 \\ SW12 & SW22 & \dots & SWn2 \\ SW13 & SW23 & \dots & SWn3 \\ SW14 & SW24 & \dots & SWn4 \\ SW15 & SW25 & \dots & SWn5 \\ SW16 & SW26 & \dots & SWn6 \\ SW17 & SW27 & \dots & SWn7 \end{bmatrix}_{7 \times n}$ The sorting algorithm sorts the columns of $SW_{matrix}$ twice. Once based on the SOC of battery cells and others based on the SOC of UCs, they name them A and B, respectively. The order of batteries in the decreasing order of battery voltage is $V_{b4} > V_{b3} > V_{b1} > V_{b2} \dots > V_{b8}$ and that of UCs is $V_{UC3} > V_{UC2} > V_{UC4} > V_{UC1} \dots > V_{UC8}$ then the respective A and B matrix would be: $A = \begin{bmatrix} SW(:,4) \\ SW(:,3) \\ SW(:,1) \\ SW(:,2) \\ \dots \\ \dots \\ \dots \\ SW(:,8) \end{bmatrix}_{n \times 1} \quad B = \begin{bmatrix} SW(:,3) \\ SW(:,2) \\ SW(:,4) \\ SW(:,1) \\ \dots \\ \dots \\ \dots \\ SW(:,8) \end{bmatrix}_{n \times 1}$ Where, $SW(:,n) = [SWn1 \ SWn2 \ SWn3 \ SWn4 \ SWn5 \ SWn6 \ SWn7]$	<b>Step 8</b>	Matrix C contains the SM, which needs to provide both UC and Battery $If V_{req} > 0$ $n = 1: order(C)$ $C(n) = [1 \ 0 \ 0 \ 1 \ 1 \ 0 \ 0]$ $n = n + 1$ $else$ $n = 1: orcer(C)$ $C(n) = [0 \ 1 \ 1 \ 0 \ 0 \ 1 \ 1]$ $n = n + 1$ $End$
<b>Step 4</b>	The algorithm then picks the top 3 battery cells from matrix A and the top 2 UC cells from matrix B and creates a new matrix A' and B'. A' contains SMs that provide $V_B$ and B' contains SMs providing $V_{UC}$ . In this case study, A' and B' would be: $A' = \begin{bmatrix} SW(:,4) \\ SW(:,3) \\ SW(:,1) \end{bmatrix}_{3 \times 1} \quad B' = \begin{bmatrix} SW(:,3) \\ SW(:,2) \end{bmatrix}_{2 \times 1}$	<b>Step 9</b>	Default state of each SM is $[1 \ 1 \ 0 \ 0 \ [previous \ state]]$ Thus, the updated Switch matrix for $k + 1^{th}$ instant would be $SW_{matrix}(k+1) = \begin{bmatrix} 1 & 1 & 1 & 1 & & 1 \\ 0 & 0 & 0 & 0 & & 1 \\ 0 & 0 & 0 & 0 & & 0 \\ 1 & 1 & 1 & 1 & \dots & 0 \\ 0 & 0 & 1 & 0 & & SWn5(k) \\ 0 & 1 & 0 & 0 & & SWn6(k) \\ 1 & 0 & 0 & 1 & & SWn7(k) \end{bmatrix}_{7 \times n}$
<b>Step 5</b>	A third matrix, C which is generated by intersecting the A' and B' matrix. $C = A' \cap B'$ In this example, $C = [SW(:,3)]$		
<b>Step 6</b>	Matrix B.O. is created, which contains the switching states for SM, which needs to turn battery only, $BO = A' - C$ $BO = \begin{bmatrix} SW(:,4) \\ SW(:,1) \end{bmatrix}$ $If V_{req} > 0$ $n = 1: order(BO)$ $BO(n) = [1 \ 0 \ 0 \ 1 \ 0 \ 0 \ 1]$ $n = n + 1$ $else$ $n = 1: orcer(BO)$ $BO(n) = [0 \ 1 \ 1 \ 0 \ 0 \ 0 \ 1]$ $n = n + 1$ $End$		

## REFERENCES

- [1] Kuperman I. Aharon "Battery-ultracapacitor hybrids for pulsed current loads: A review" *Renew. Sustain. Energy Rev.* vol. 15 pp. 981-992 2011.
- [2] K. J. Frankforter, M. I. Tejedor-Tejedor, M. A. Anderson and T. M. Jahns, "Investigation of Hybrid Battery/Ultracapacitor Electrode Customization for Energy Storage Applications with Different Energy and Power Requirements using HPPC Cycling," *IEEE Trans. Ind. Appl.* vol. 56, no. 2, pp. 1714-1728, March-Apr. 2020.
- [3] R. A. Dougal, S. Liu and R. E. White, "Power and life extension of battery-ultracapacitor hybrids," *IEEE Trans. Compon. Packag. Manuf. Technol.*, vol. 25, no. 1, pp. 120-131, March 2002.
- [4] I. Aharon and A. Kuperman, "Topological Overview of Powertrains for Battery-Powered Vehicles With Range Extenders," *IEEE Trans. Power Electron.*, vol. 26, no. 3, pp. 868-876, March 2011.
- [5] J. Cao, and A. Emadi, "A new battery/ultracapacitor hybrid energy storage system for electric, hybrid, and plug-in hybrid electric vehicles," *IEEE Trans. Power Electron.*, vol. 27, no. 1, pp. 122-132, Jan. 2012.
- [6] M. Momayyezani, D. B. W. Abeywardana, B. Hredzak and V. G. Agelidis, "Integrated Reconfigurable Configuration for Battery/Ultracapacitor Hybrid Energy Storage Systems," *IEEE Trans. on Energy Convers.*, vol. 31, no. 4, pp. 1583-1590, Dec. 2016.
- [7] A. Bharadwaj, S. Maiti, N. Dhal, and S. Chakraborty "Control and sizing of modular multilevel converter-based STATCOM with hybrid energy storage system for large-scale integration of wind farms with the grid," *Electrical Engineering* 101, no. 3, pp. 743-757, Sep. 2019.
- [8] Z. Zheng, K. Wang, L. Xu and Y. Li, "A Hybrid Cascaded Multilevel Converter for Battery Energy Management Applied in Electric Vehicles," *IEEE Trans. on Power Electron.*, vol. 29, no. 7, pp. 3537-3546, July 2014.
- [9] M. Quraan T. Yeo P. Tricoli "Design and control of modular multilevel converters for battery electric vehicles" *IEEE Trans. Power Electron.* vol. 31 no. 1 pp. 507-515 Jan. 2016.
- [10] Y. Yuanmao, K. W. E. Cheng and Y. P. B. Yeung, "Zero-Current Switching Switched-Capacitor Zero-Voltage-Gap Automatic Equalization System for Series Battery String," *IEEE Trans. on Power Electron.*, vol. 27, no. 7, pp. 3234-3242, July 2012.
- [11] L. A. Tolbert, Fang Zheng Peng, T. Cunyngham and J. N. Chiasson, "Charge balance control schemes for cascade multilevel converter in hybrid electric vehicles," *IEEE Trans. on Ind. Electron.*, vol. 49, no. 5, pp. 1058-1064, Oct. 2002.
- [12] M. Quraan P. Tricoli S. D'Arco L. Piegari "Efficiency assessment of modular multilevel converters for battery electric vehicles" *IEEE Trans. Power Electron.* vol. 32 no. 3 pp. 2041-2051, 2017.
- [13] M. Quraan T. Yeo P. Tricoli "Design and control of modular multilevel converters for battery electric vehicles" *IEEE Trans. Power Electron.* vol. 31 no. 1 pp. 507-515 Jan. 2016.
- [14] C. Gan Q. Sun J. Wu W. Kong C. Shi Y. Hu "MMC-based SRM drives with decentralized battery energy storage system for hybrid electric vehicles" *IEEE Trans. Power Electron.* vol. 34 no. 3 pp. 2608-2621 Mar. 2019.
- [15] D. Ronanki S. S. Williamson "Modular multilevel converters for transportation electrification: Challenges and opportunities" *IEEE Trans. Transport. Electrification.* vol. 4 no. 2 pp. 399-407, 2018.
- [16] J. Shen and A. Khaligh, "A Supervisory Energy Management Control Strategy in a Battery/Ultracapacitor Hybrid Energy Storage System," *IEEE Trans. on Transport. Electrification.* vol. 1, no. 3, pp. 223-231, Oct. 2015.
- [17] K. Alobeidli V. Khadkikar "A new ultracapacitor state-of-charge control concept to enhance battery lifespan of dual storage electric vehicles" *IEEE Trans. Veh. Technol.* vol. 67 no. 11 pp. 10470-10481 Nov. 2018
- [18] H. Yin W. Zhou M. Li C. Ma C. Zhao "An adaptive fuzzy logic-based energy management strategy on battery/ultracapacitor hybrid electric vehicles" *IEEE Trans. Transport. Electrification.* vol. 2 no. 3 pp. 300-311 Sep. 2016.
- [19] J. I. Metri, H. Vahedi, H. Y. Kanaan and K. Al-Haddad, "Real-Time Implementation of Model-Predictive Control on Seven-Level Packed U-Cell Inverter," *IEEE Trans. on Ind. Electron.*, vol. 63, no. 7, pp. 4180-4186, July 2016.
- [20] J. Qin and M. Saeedifard, "Predictive control of a modular multilevel converter for a back-to-back HVDC system," *IEEE Trans. Power Del.*, vol. 27, no. 3, pp. 1538-1547, Jul. 2012.
- [21] J. Moon, J. Gwon, J. Park, D. Kang and J. Kim, "Model Predictive Control With a Reduced Number of Considered States in a Modular Multilevel Converter for HVDC System," *IEEE Trans. on Power Del.*, vol. 30, no. 2, pp. 608-617, April 2015.
- [22] Z. Gong, P. Dai, X. Yuan, X. Wu and G. Guo, "Design and Experimental Evaluation of Fast Model Predictive Control for Modular Multilevel Converters," *IEEE Trans. on Ind. Electron.*, vol. 63, no. 6, pp. 3845-3856, June 2016.
- [23] H. Mahmoudi, M. Aleenejad and R. Ahmadi, "Modulated Model Predictive Control of Modular Multilevel Converters in VSC-HVDC Systems," *IEEE Trans. on Power Del.*, vol. 33, no. 5, pp. 2115-2124, Oct. 2018.
- [24] Y. Yang et al., "Multiple-Voltage-Vector Model Predictive Control With Reduced Complexity for Multilevel Inverters," *IEEE Trans. on Transport. Electrification.* vol. 6, no. 1, pp. 105-117, March 2020.
- [25] Z. Mynar, L. Vesely and P. Vaclavik, "PMSM Model Predictive Control With Field-Weakening Implementation," *IEEE Trans. on Ind. Electron.*, vol. 63, no. 8, pp. 5156-5166, Aug. 2016.
- [26] J. Liu, C. Gong, Z. Han and H. Yu, "IPMSM Model Predictive Control in Flux-Weakening Operation Using an Improved Algorithm," *IEEE Trans. on Ind. Electron.*, vol. 65, no. 12, pp. 9378-9387, Dec. 2018.
- [27] M. M. Hoque, M. A. Hannan, A. Mohamed, and A. Ayob. "Battery charge equalization controller in electric vehicle applications: A review." *Renew. and Sust. Energy Reviews*, No. 75, pp. 1363-1385, Aug. 2017.
- [28] S. Moore, and P. Schneider, "A Review of Cell Equalization Methods for Lithium Ion and Lithium Polymer Battery Systems," *SAE Technical Paper*, No. 2001-01-0959, 2001
- [29] M. Muneeb Ur Rehman, F. Zhang, R. Zane and D. Maksimovic, "Design and control of an integrated BMS/DC-DC system for electric vehicles," in *proc. 2016 IEEE 17th Workshop on Control and Modeling for Power Electron. (COMPEL)*, Trondheim, 2016, pp. 1-7.
- [30] S. Li, C. C. Mi and M. Zhang, "A High-Efficiency Active Battery-Balancing Circuit Using Multiwinding Transformer," *IEEE Trans. on Ind. Appl.*, vol. 49, no. 1, pp. 198-207, Jan.-Feb. 2013.
- [31] Y. Yuanmao, K. W. E. Cheng and Y. P. B. Yeung, "Zero-Current Switching Switched-Capacitor Zero-Voltage-Gap Automatic Equalization System for Series Battery String," *IEEE Trans. on Power Electron.*, vol. 27, no. 7, pp. 3234-3242, July 2012.
- [32] M. Kim, C. Kim, J. Kim and G. Moon, "A Chain Structure of Switched Capacitor for Improved Cell Balancing Speed of Lithium-Ion Batteries," *IEEE Trans. on Ind. Electron.*, vol. 61, no. 8, pp. 3989-3999, Aug. 2014.
- [33] Z. Zheng, K. Wang, L. Xu and Y. Li, "A Hybrid Cascaded Multilevel Converter for Battery Energy Management Applied in Electric Vehicles," *IEEE Trans. on Power Electron.*, vol. 29, no. 7, pp. 3537-3546, July 2014.
- [34] M. Quraan, T. Yeo and P. Tricoli, "Design and Control of Modular Multilevel Converters for Battery Electric Vehicles," *IEEE Trans. on Power Electron.*, vol. 31, no. 1, pp. 507-517, Jan. 2016.
- [35] D. Ronanki and S. S. Williamson, "Modular Multilevel Converters for Transportation Electrification: Challenges and Opportunities," *IEEE Trans. on Transport. Electrification.* vol. 4, no. 2, pp. 399-407, June 2018.
- [36] Z. Gao and Q. Lu, "A Hybrid Cascaded Multilevel Converter Based on Three-Level Cells for Battery Energy Management Applied in Electric Vehicles," *IEEE Trans. on Power Electron.*, vol. 34, no. 8, pp. 7326-7349, Aug. 2019.
- [37] S. S. George and M. O. Badawy, "A Modular Multi-Level Converter for Energy Management of Hybrid Storage System in Electric Vehicles," in *proc. 2018 IEEE Transport. Electrification. Conf. and Expo (ITEC)*, Long Beach, CA, 2018, pp. 336-341.
- [38] M. O. Badawy, T. Husain, and J. A. De Abreu-Garcia, "Integrated Control of an IPM Motor Drive and a Novel Hybrid Energy Storage System for Electric Vehicles," *IEEE Trans. Ind. Appl.*, 2017, vol. 53, pp. 5810-5819.
- [39] H. Akagi, "Classification, Terminology, and Application of the Modular Multilevel Cascade Converter (MMCC)," *IEEE Trans. Power Electron.*, vol. 26, no. 11, pp. 3119-3130, Nov. 2011.
- [40] L. M. Tolbert, Fang Zheng Peng and T. G. Habetler, "Multilevel converters for large electric drives," *IEEE Trans. on Ind. Appl.*, vol. 35, no. 1, pp. 36-44, Jan.-Feb. 1999.
- [41] G. Plett, Battery Management Systems Volume II: Equivalent-Circuit Methods. Norwood, MA: Artech House, 2016.
- [42] G. Plett, Battery Management Systems Volume I: Battery Modeling. Norwood, MA: Artech House, 2015.
- [43] Ahmed, R., Gazzarri, J., Onori, S., Habibi, S. et al., "Model-Based Parameter Identification of Healthy and Aged Li-ion Batteries for Electric Vehicle Applications," *SAE Int. J. Alt.Power.* 4(2):2015.
- [44] L. Sepulchre, M. Fadel, M. Pietrzak-David and G. Porte, "New high speed PMSM flux-weakening strategy," in *proc. 2016 19th International Conference on Electrical Machines and Systems (ICEMS)*, Chiba, 2016, pp. 1-6.
- [45] P. Vaclavik and P. Blaha "Interior Permanent Magnet Synchronous Machine High Speed Operation using Field Weakening Control Strategy," in *proc. 12th WSEAS Conference on SYSTEMS*, Heraklion, Greece, July 22-24, 2008
- [46] Xuecong Xu, et al., "Predictive speed control of interior permanent magnet synchronous motor with maximum torque per ampere control strategy," in *proc. 36th Chinese Control Conference*, Dalian, China, Jul. 2017
- [47] M. Sharma, C. Hernandez, and M.O. Badawy. "Application of Model Predictive control in Modular Multilevel converter for MTPA operation and SOC Balancing," in *proc. 2018 IEEE 19th Workshop on Control and Modeling for Power Electron. (COMPEL)*, Pedua, Italy, pp. 1-8 June 2018
- [48] K. W. E. Cheng, B. P. Divakar, H. Wu, K. Ding, and H. F. Ho, "Battery-Management System (BMS) and SOC Development for Electrical Vehicles," *IEEE Trans. on Veh. Technol.*, vol. 60, no. 1, pp. 76-88, Jan. 2011.





**Mohamed O. Badawy** (M'16) received the B.Sc. degree in electrical engineering from Cairo University, Cairo, Egypt, and the M.Sc. and Ph.D. degrees in electrical and computer engineering from the University of Akron, OH, USA, in 2007, 2012, and 2016, respectively. Since 2016, he has been an Assistant Professor in the Department of Electrical Engineering, San Jose State University (SJSU), C.A., USA. Dr. Badawy is the director of the center of power electronic converters at SJSU. His research interests are power electronic configurations and control structures for advanced electric vehicles and renewable energy systems. Dr. Badawy has been an organizing committee member for several IEEE conferences, a reviewer for several IEEE Journals and Transactions. He currently serves as an Associate Editor for IEEE Transactions on Industry Applications.



**Mohit Sharma** received his B.E. degree in Electrical and Electronics Engineering from Panjab University, Chandigarh, India, in 2015, and his M.Sc. degree in Electrical Engineering from San Jose State University, San Jose, CA, in 2018. He is currently a Power Electronics Engineer at ChargePoint, working on AC and DC charging systems for Electric Vehicles.

His current research interests are power electronic converters' design for electric vehicle charging systems and their control structures.

**Carlos Hernandez** earned his B.Sc. in Electrical Engineering from the University of California Riverside and his M.Sc. in Electrical Engineering from San Jose State University in 2016 and 2018. His



research interests include machine drives and control, general power electronics, and applications of modular multilevel converters.



**Ali Elrayyah** (M'15) received the B.Sc. degree in electrical and electronics engineering from the University of Khartoum, Khartoum, Sudan, in 2003, the M.Sc. degree in systems engineering from King Fahd University of Petroleum and Minerals (KFUPM), Dhahran, Saudi Arabia, in 2009, and the Ph.D. degree from University of Akron, Akron, OH, USA, in 2013. He is currently a Scientist at Qatar Environment and Energy Research Institute. His research interests include alternative energy systems and control of standalone and utility-interactive energy systems.



**Joshua Coe** received his M.Sc. degree in Electrical Engineering from San Jose State University, San Jose, CA, in 2019. He is currently a Test Engineer for Lucid Motors, managing onboard charging tests. His research interests include power converters' design for electric vehicle drivetrains and electric vehicle charging stations.